Journal of The Electrochemical Society, **161** (13) H3117-H3129 (2014)
0013-4651/2014/161(13)/H3117/13/$31.00 © The Electrochemical Society

JES Focus Issue in Recognition of Adam Heller and His Enduring Contributions to Electrochemistry

Semiconductor Surface Transformations for Photoelectrochemical Energy Conversion

Hans J. Lewerenz[z]

Joint Center for Artificial Photosynthesis, California Institute of Technology, Pasadena, California 91125, USA

The issue of photoelectrode stability, while simultaneously maintaining efficient operation in aqueous solutions, is addressed for energy converting half cells and complete photoelectrocatalytic structures. The historical development of stability concepts, their realization and recent advances are described. Examples are presented that span the time from the inception of photoelectrochemical energy conversion to present day's renewed interest in storable solar energy. The application of (photo)corrosion processes for in-situ synthesis of protective coatings is described and chemical and electronic analyses of the interphases formed are given. Future development and innovation routes will be discussed.

Manuscript submitted October 6, 2014; revised manuscript received November 10, 2014. Published December 3, 2014. *This paper is part of the JES Focus Issue in Recognition of Adam Heller and His Enduring Contributions to Electrochemistry.*

The early days of light-induced processes at the solid-electrolyte interface were characterized by a series of fascinating effects. They encompass fundamental investigations of semiconductor-electrolyte junctions,[1,2] the first light-assisted water splitting,[3] photoemission from metals into solution,[4,5] hot electron processes[6,7] and the first carbon dioxide reduction at illuminated semiconductors.[8,9] The conceptual basis of energy conversion at the solid-liquid junction was provided by Gerischer in 1975 when the rectifying nature of the semiconductor-redox electrolyte contact was outlined.[1] The elegance of formation of a conformal contact, simply by immersion of the samples into solution, was, however, neutralized by interfacial reactivity that gives rise to photocorrosion.[10,11] In the early assessment of stability of semiconductors at electrolyte junctions, thermodynamic decomposition potentials were introduced and their energy relation relative to the semiconductor band edges was analyzed.[10,12] It soon turned out that stability is a predominant and major issue in photoelectrochemical energy conversion in both the photovoltaic and photoelectrocatalytic modes. Early development of stable photoelectrodes, based on the group VIb transition metal dichalcogenides,[13–15] which are also characterized by high absorptivity, was compromised by the problem of scalable preparation of efficient electrodes. Technologically advanced semiconductors from the III-V and II-VI groups typically showed rather high conversion efficiencies[16–18] but, also, often pronounced photocorrosion.[19] A promising approach for stabilization was developed by the Bell Laboratories group where ~ 10% efficient InP photocathodes had been operated for extended time in aqueous solution.[20] The employed conditioning method resulted in the formation of interfacial films[21] that enabled electron transfer but that blocked access of solution components to the absorber surface thereby suppressing the corrosion reactions.

In this text, fundamental aspects and recent developments and advances of this method will be outlined and discussed. Basic concepts on stability and photocorrosion are presented first, followed briefly by a discussion of carrier transport across interfacial films. A subsequent section describes the chronological development of the field in case studies, followed by a synopsis on perspectives for light-induced water splitting and beyond that also addresses simultaneous water oxidation and carbon dioxide reduction.

Stability Concepts

The original concept of Gerischer describes semiconductor stability by calculating energy levels associated with the respective corrosion reactions,[10] ${}_{n,p}E_{dec}$ (superscripts n and p refer to anodic and cathodic reactions) and relating them to the semiconductor band edges and the Quasi Fermi levels under illumination.[22] This concept describes the fundamental conditions which lead to photocorrosion; it is primarily based on thermodynamic considerations, establishing energy relations, but has been extended to include kinetic aspects.[10] The correlation of redox potentials of decomposition reactions with the band edges of semiconductors allows determination whether a given material in the respective electrolyte would be susceptible to anodic and/or cathodic corrosion. The concept has been expanded to illuminated semiconductors where the free energy of holes and electrons enter the picture.

The anodic and cathodic decomposition of a compound semiconductor is typically written as

$$MX + zh^+ + aq \rightarrow M_{aq}^{z+} + X \qquad (E_h > {}_pE_{dec}) \qquad [1a]$$

$$MX + ze^- + aq \rightarrow M + X_{aq}^{z-} \qquad (E_e < {}_nE_{dec}) \qquad [1b]$$

Eqns. 1a, 1b establish a redox potential (here mostly considered as energy to align with the semiconductor energy band structure) and they proceed if the energy of the holes, E_h, in the anodic corrosion process is smaller (potential more positive) than the thermodynamic potential of the redox reaction, ${}_nE_{dec}$. For cathodic decomposition, the electrons must possess higher energy than the cathodic decomposition redox energy, ${}_nE_{dec}$. The corrosion reactions prevail under the energetic conditions given by the inequalities on the right hand side of the electrochemical relations in eqn. (1). It should be noted that these reactions can lead to further species upon reaction of products with the solute, a fact that will become relevant further below. An example for a more complex corrosion reaction is the anodic dissolution of GaAs that can occur by anodic polarization in the dark, forming an accumulation layer with a high surface concentration of holes or by illumination where light-induced holes exist at the positively charged surface,

$$GaAs + 6h^+ + H_2O + aq \rightarrow Ga_{aq}^{3+} + AsO_2^- + 4H_{aq}^+ \qquad [2]$$

which results in dissolution of the cation and oxidation of the anion. The solubility of the products formed defines whether a system will corrode until dissolved or whether the reaction stops when charges can no longer be transferred through an insulating phase. Whereas eqn. 2 describes the former process, eqn. 3 shows formation of a solid phase at the surface via anodic corrosion of the semiconductor CdS

$$CdS + 2h^+ + aq \rightarrow Cd_{aq}^{2+} + S \qquad [3]$$

The corrosion reaction might also, however, result in the formation of a conducting phase or an insulator which exhibits defect states and -bands that allow charge transport through the layer.

It becomes obvious that less soluble corrosion products might be used to form interfacial films of desired properties if one judiciously

[z]E-mail: lewerenz@caltech.edu

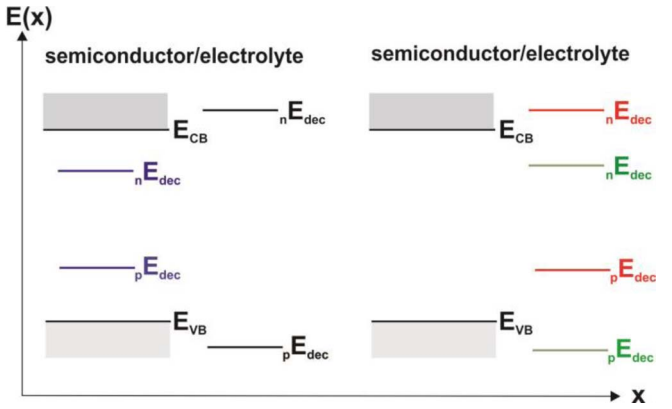

Figure 1. Energy relations for semiconductor stability at the electrolyte contact; ${}_{n,p}E_{dec}$, anodic and cathodic decomposition levels, respectively (see text).

chooses solution composition, potential, time and illumination level, for example. Now, how does one arrive at redox potentials of corrosion reactions and be able to compare them with semiconductor energy levels? One combines eqn. (1) with the redox reaction of the standard hydrogen electrode using the reaction as source of electrons or holes

$$zH^+_{aq} + ze^- \leftrightarrow \frac{z}{2}H_2 + aq \quad \text{(electrons)} \qquad [4]$$

For cathodic decomposition one obtains with eqns. 1b and 4

$$MX + \frac{z}{2}H_2 + aq \rightarrow M + X^{z-}_{aq} + zH^+_{aq} \qquad [5]$$

transforming the electrochemical relation into a chemical reaction for which ΔG^0 can be determined by calculation or from tables.[23,24] The decomposition potential for our example of a cathodic process is then given by

$${}_nV_{dec} = -\frac{\Delta G_{cath}}{zF} \qquad [6]$$

where F denotes Faraday's constant. The relative energetic position of these redox potentials $V_{R,O}$, with respect to the semiconductor energy bands is obtained by relating the Fermi level of an electrode to the vacuum work function of the standard hydrogen electrode via

$$E_F = -e_0V_{R,O} + E_{SHE} \qquad [7]$$

The work function of the SHE is about −4.5 eV± 0.2 eV and, using these data, one obtains the energies for the redox reactions at the physics vacuum scale. The principle is shown in Fig. 1 where the decomposition energy levels are related to semiconductor conduction- and valence band edges. The stability criteria are: for ${}_nE_{dec} > E_{CB}$, a semiconductor is cathodically stable since the electrons at the conduction band edge are not energetic enough to induce the corrosion reaction; if ${}_nE_{dec} < E_{CB}$ cathodic decomposition occurs; equivalent considerations hold for the valence band and ${}_pE_{dec}$.[5]

The left hand side shows the situation for anodically and cathodically stable semiconductors (decomposition energy levels: black) and, in blue color, the case where both levels are energetically located within the energy gap, hence such a material would be unstable for both anodic and cathodic corrosion. The red levels in the right hand side of Fig. 1 indicate cathodic stability and anodic corrosion and vice versa for the green labeled levels. It should be noted that in the case of the stable layered compound MoS_2, these thermodynamic considerations give misleading results since MX_2 (M = W, Mo; X = S, Se, Te) semiconductors derive their stability from peculiarities of the band structure[25] that are not included in the concept. The fundamental energy gap results from intrametallic d-bands, therefore the M-X bonding is not affected or minimally affected (depending on remnant hybridization) by the interactions of electrons and holes with the electrolyte.

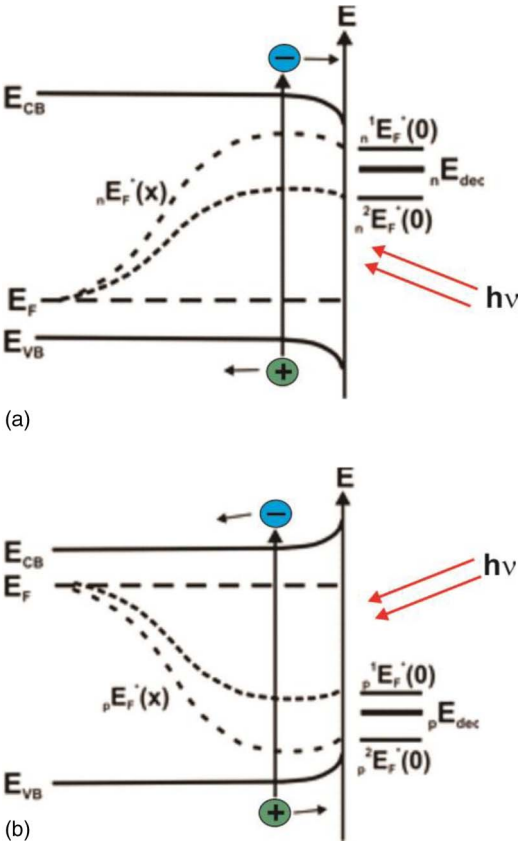

Figure 2. Stability assessment by the position of quasi Fermi levels and anodic and cathodic decomposition levels; (a): p-semiconductor with decomposition level above ${}_n{}^2E_F{}^*(0)$, indicating stability but below ${}_n{}^1E_F{}^*(0)$, indicating photocorrosion; (b) photoanodes, with according relations for ${}_p{}^2E_F{}^*(0)$ and ${}_p{}^1E_F{}^*(0)$ where stable operation is observed for ${}_p{}^1E_F{}^*(0)$.

Under illumination, stability has been described using the position of quasi Fermi levels (QFL) at the surface in relation to decomposition levels. QFLs describe the change in population of the conduction and valence bands due to illumination, leading to a change of the concentration of minority and majority carriers. Since photo-effects are minority carrier dominated, we write for an n-type semiconductor the hole excess carrier concentration $p \rightarrow p^* = p + \Delta p(x)$ (eqn. 8)

$${}_pE^*_F(x) = E_F - kT\ln\frac{p^*(x)}{p} = E_F - kT\ln\left(1 + \frac{\Delta p(x)}{p}\right) \qquad [8]$$

and for p-semiconductors where the bulk equilibrium carrier concentration changes from n to n* the quasi Fermi level reads

$${}_nE^*_F(x) = E_F + kT\ln\frac{n^*(x)}{n} = E_F + kT\ln\left(1 + \frac{\Delta n(x)}{n}\right) \qquad [9]$$

Fig. 2 shows energy relations including the band edges, quasi Fermi levels at different illumination levels and decomposition energies for p- and n-type semiconductors. The curvature of the QFLs indicates losses in excess carrier concentration due to surface/interface recombination. For higher light intensity, the QFLs are energetically further away from the bulk Fermi level, as seen by the more open dashed lines in Fig. 2. Also, the downward bending of the QFL is increased assuming an increased surface recombination at higher light levels. The figure indicates that thermodynamic stability can be a function of illumination intensity and surface recombination velocity, S_r.

The above discussion addressed the free energy change averaged over the single steps of a complex decomposition reaction as, for example, shown in eqn. 2. Analysis of reaction kinetics, in contrast, requires individual consideration of all reaction steps, both chemical and electrochemical. The rate determining step (rds) will, of course,

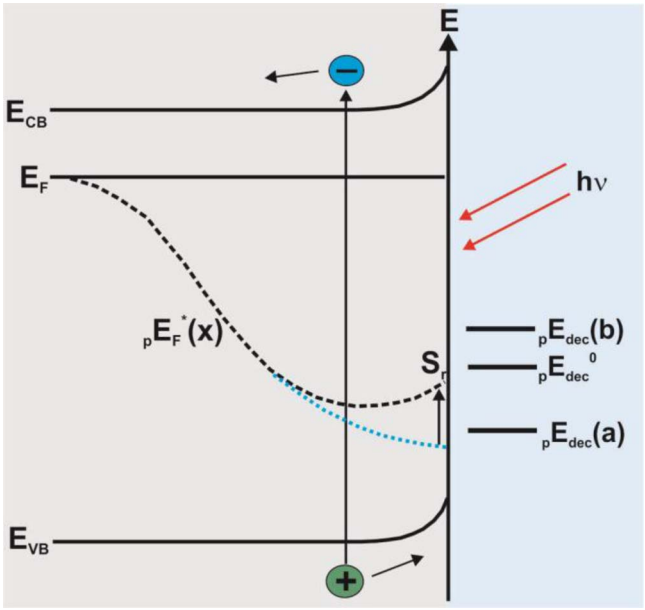

Figure 3. Energy schematic for anodic photocorrosion including phenomenologically the surface recombination at a given light intensity; $_pE_{dec}(a)$ rds, $_pE_{dec}(b)$ second partial corrosion step, $_pE_{dec}^0$ thermodynamic level for overall reaction (see text).

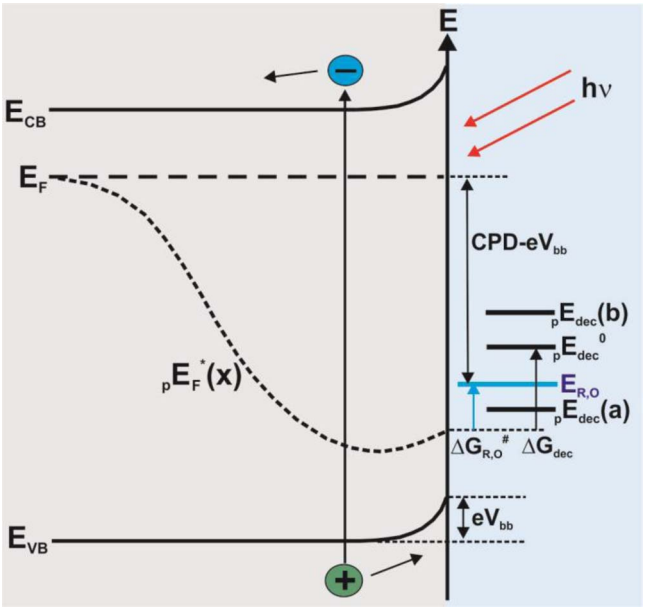

Figure 4. Energy schematic for an illuminated semiconductor in contact with a redox couple at a potential near the maximum power point with most of the band bending reversed; CPD, contact potential difference;□$\Delta G_{R,O}$ and ΔG_{dec} denote the energy difference of QFL at x = 0 with respect to the redox reaction $E_{R,O}$ and relative to the thermodynamic potential of the corrosion reaction, respectively; also shown are the decomposition levels for two partial reactions (a) and (b) that are located below and above the redox energy, respectively.

be the one with the highest activation barrier. For a decomposition reaction that consists of two steps where the first step is (typically) rate determining, the energy schematic in Fig. 3 shows that the overall stability of the semiconductor can be different than by just analyzing the overall reaction and that, as above in Fig. 2, the illumination level and S_r contribute.

The QFL at the surface for zero surface recombination is described by the blue dotted line and, with increasing S_r, the profile given by the black dashed line is obtained. With the decomposition level (a) located below the black dashed line, the corrosion reaction would not commence for high surface recombination although the thermodynamic level is located above the QFL at the surface. With reduced surface recombination, the QFL (blue dotted line) is energetically located below the level for the first reaction step and photocorrosion will prevail.

It should be noted here that when a semiconductor - redox electrolyte system is operated as a photovoltaic or photoelectrocatalytic half cell with an appreciable fill factor, the maximum power point (mpp) will typically be located a few tenths of a volt positive from the open circuit potential (n-semiconductor). Therefore, the mpp of each respective system defines also the susceptibility to photocorrosion via the position of the QFL relative to the rds of the corrosion reaction. For the application below, we note that near open circuit, photocorrosion is most likely as the QFL of the minority carriers exhibits the largest distance to the majority QFL (not discussed here). Also, the dark current increases exponentially due to the increase of the majority carrier concentration. This current is of opposite sign and is cathodic for n-semiconductors. At open circuit, the currents for oxidation and reduction processes are equal and the net current vanishes. The maximum photovoltage of the absorber is given by the difference of the QFLs at the surface, $\Delta_nE_F^*(x = 0) - \Delta_pE_F^*(x = 0) = \Delta E_F^*(0)$. The contact potential difference and, in an ideal case without significant density of surface states, the maximum band bending, however, is determined by the difference of the semiconductor bulk Fermi level and the redox level in solution. Fig. 4 depicts the energetics for operation of a half-cell near mpp. Besides the redox level, a two-step corrosion reaction has been assumed to exist where the rds is located below the redox couple electrochemical potential. The reaction dynamics can be described by rate theory[26] using the free energies ΔG, as labeled in Fig. 4. They enter the reaction rate exponentially and, according to the schematic in Fig. 4, the decomposition reaction should proceed faster than the redox reaction as it is more negative in potential. However, since the first step of that former lies energetically below the $E_{R,O}$, the photocorrosion reaction will proceed at a smaller rate but will eventually result in semiconductor decomposition or passivity.

What approaches exist or can be envisaged for stability under operation as a photovoltaic electrochemical cell and as a photoelectrocatalytic system? In the former case, a rectifying contact forms with the redox electrolyte. Typically, the energy level of the redox couple lies within the bandgap of a semiconductor with high absorption in the visible-to-IR spectral range, e.g. roughly between 1 eV–2 eV. For this energy range, the theoretical solar conversion efficiencies, η, are in the range of 20% – 30% with a maximum η ∼ 30% at 1.4 eV (AM 1.5).[61]

A difference in stability related to the photoelectrocatalytic mode can be attributed to kinetics since fast single-electron transfer redox couples (such as $V^{2+/3+}$) can compete favourably with corrosion reaction, particularly if the decomposition level is located energetically below (n-type semiconductor) or above (p-type) the respective redox level. For H_2 or O_2 evolution, steps of the multi-electron transfer processes compete with those of the corrosion reactions and the susceptibility to photodecomposition is generally increased. In addition, hydrogen evolution is known to result in diffusion of H into the material and, acting as donors, p-semiconductors can become intrinsic and show reduced photoresponse due to reduced band bending.[27]

Carrier Transport across Interphases

At first glance, the preparation of tunnel junctions, which isolate the semiconductor surface from the electrolyte while allowing efficient electron tunneling through the interfacial layer appears promising. This approach has found numerous applications in microelectronics, for example, in field effect transistors.[28] Real surfaces, however, are not atomically flat and possess terraces, terrace edges and -steps as well as kink sites. Therefore, the deposition procedure of such ultrathin film needs to establish high conformity, following the surface

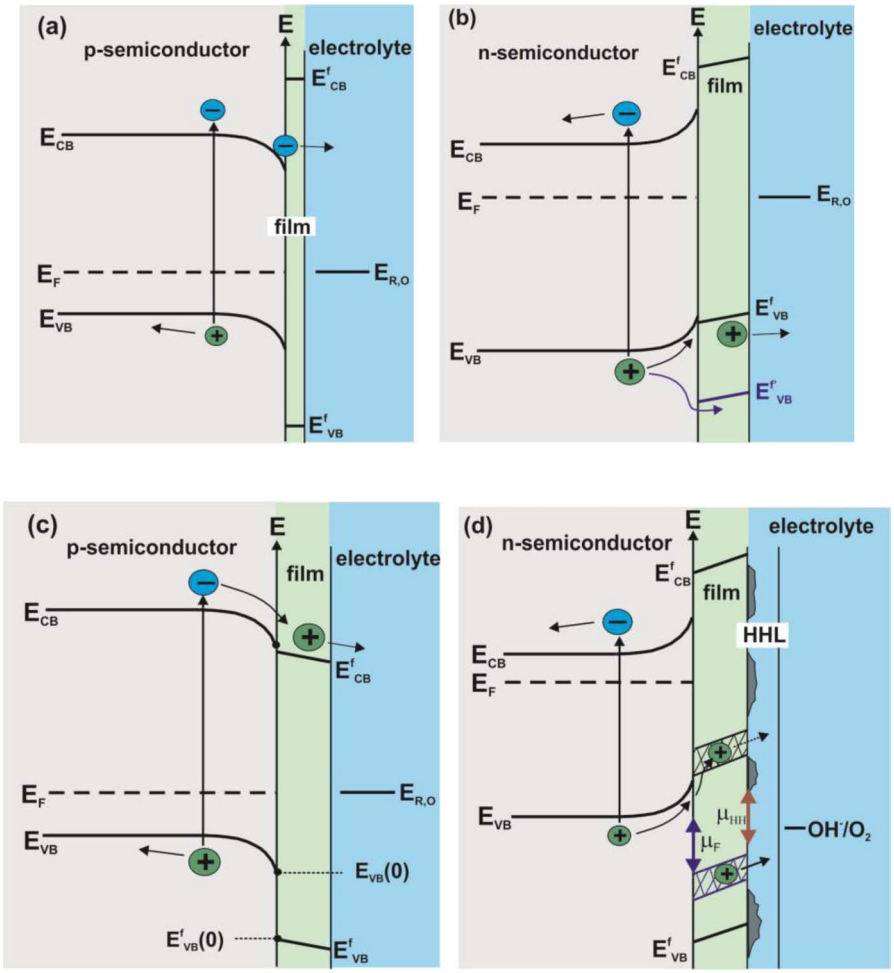

Figure 5. Energy band diagram schematics for semiconductor-interfacial film-catalyst-redox electrolyte contacts; (a) film with tunneling thickness, d_t for a p-type absorber; (b) film with $d > d_t$ for an n-type absorber; (c) as in (b) for p-type absorber, (d) assuming a defect band in the gap of the protection layer; E^f_{CB}, E^f_{VB}, film conduction, valence band respectively; hatched areas indicate defect bands, $\square\mu_F$ interface dipole at the semiconductor-film contact; $\square\mu_{HH}$ dipole at the metal-solution interface (Helmholtz layer); green islands at the film surface: metallic electrocatalyst; also shown is the thermodynamic potential for oxygen evolution in alkaline electrolyte (see text).

corrugation on an atomic level. Processes that have proven to be conformal enough are ALD and in-situ electrochemical interphase formation.[29,30] With films of tunneling thickness (Fig. 5a), alignment of the energy bands with those of the light absorber is not necessary. If one prepares interphases with thickness that exceed the ballistic electron transport limit, energy bands have to be aligned to allow efficient carrier transport along band edges (Fig. 5b, 5c).

If films are thicker than the tunneling thickness, d_t, charge carrier transport can occur through the valence and conduction band or via defects states with energy within the forbidden gap. In Fig. 5b, for n-type absorbers, the situation shown is not typically encountered because films that are corrosion resistant consist of transition metal oxides or other wide gap materials. With electron affinities ranging typically from 3.5–4eV, the valence band edges are located at 6.5–7 eV below the vacuum level. With semiconductors such as Si, GaAs, GaP, $CuInSe_2$, CdTe, the valence band edges (determined from $E_{VB} = \chi + E_g$) are located at 5.1 eV (Si) to 6 eV (CdTe). Accordingly, a spike in the valence band inhibits efficient hole transport. The energetic situation can be ameliorated by introducing interface dipoles that shift the absorber valence band downwards with respect to that of the film, thereby reducing the band discontinuity. For p-type absorbers, conduction band alignment is not uncommon.[31] Indium oxides, for example, have electron affinities around 4.5eV, hence efficient excess minority transfer from most semiconductor conduction bands becomes possible. An example has been drawn in Fig. 5c. In addition, the large discontinuity in the valence band strongly suppresses majority carrier related dark currents (j_s, reverse saturation current) since the concentration of holes at the semiconductor-film interface is $p = p_0 \exp[E^f_{VB}(0)\text{-}E_{VB}(0)]$ where $x = 0$ defines the geometrical semiconductor surface and p_0 denotes the bulk doping concentration. The photovoltage increases with decreasing j_s as $V_{ph} = (kT/q)\ln[(j_L/j_s)+1]$ (j_L light-induced current also known as Gaertner current[32]).

Fig. 5d depicts a situation that has been communicated recently.[33] Hole conduction along defects in amorphous TiO_2, prepared by ALD, has been observed in alkaline solution. The energy of photogenerated holes from n-Si is too small for oxygen evolution and the defect band close to the valence band edge of Si is energetically too high to oxidize the anions. The situation changes if one assumes an interfacial dipole, indicated by μ_F, between the absorber and the protection layer that increases the oxidative potential by moving the valence band edge downwards. A defect band would then be located below the redox potential and the light-induced holes have sufficient energy to induce the oxidation reaction including the overpotential η needed. On a pure semiconductor, η can be rather large but, with an electrocatalyst such as Ni, this value is reduced to about 0.3 V for photocurrent densities of 30 $mAcm^{-2}$ that are typical for efficient Si photoelectrodes.[33] The presence of an electrocatalyst has been assumed in Fig. 5d, shown as green islands on top of the interfacial film. If the metal covers large parts of the surface, an applied anodic voltage will shift the band edge positions of the film/semiconductor structure anodically, i.e. energetically downwards. Eventually, the defect band energy will be located below the oxygen evolution level, including the overpotential, as indicated by the red arrow, labeled μ_{HH}.

Transport phenomena related to defects have been investigated in semiconductor physics[34] but only little information exists in electrochemistry. Under the influence of a persistent electric field along the interfacial film, assumed to be a dielectric, transport could occur via the Poole-Frenkel mechanism[35] that has also been postulated in transport along polypeptide chains.[36] For a few tenths of a volt potential drop across a film of 50 nm thickness, the electric field is in the range

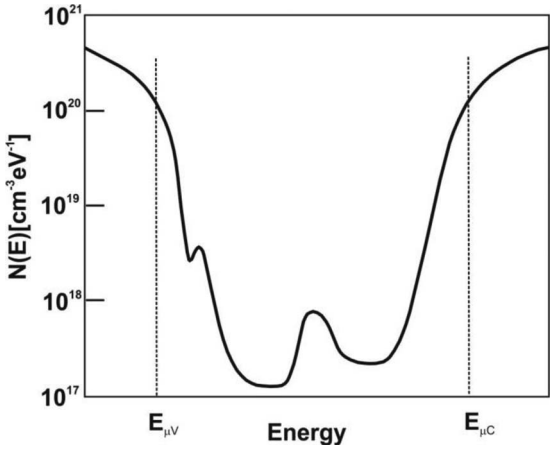

Figure 6. Density of states for an amorphous semiconductor versus energy; the mobility gap, where conduction in extended states exists, is given by $E_{\mu C}$ - $E_{\mu V}$ □, i.e. the difference in the mobility edges for electron and hole conduction.

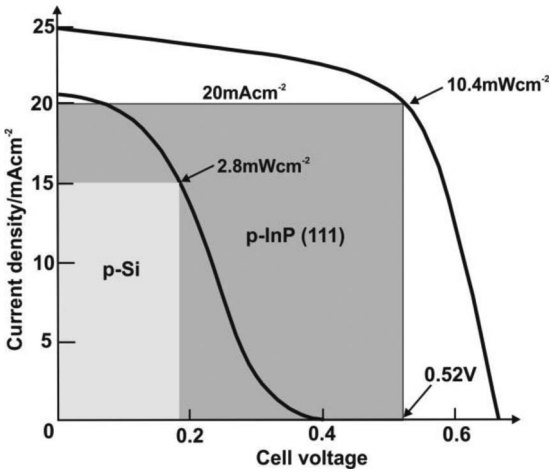

Figure 7. Historical photocurrent-voltage characteristics for InP and Si photocathodes; measurements were done in natural sunlight of 110 $mWcm^{-2}$(InP) and 101 $mWcm^{-2}$(Si); $V^{2+/3+}$-HCl redox electrolyte, C counter electrode (see text).

of $5 \cdot 10^4$ V/cm. The onset of Poole-Frenkel transport depends on the trap depth, Φ_{tr}, which enters as decisive parameter the current-voltage relationship:

$$j_{PF} = E\exp\left[-\frac{q\emptyset_{tr} + \sqrt{(qE/\epsilon)}}{kT}\right] \quad [10]$$

where E denotes the applied electric field. For insulators such as SiO_2 on SiC, with deep traps, the onset voltage is in the 10^6 V/cm range[37] and hence this mechanism can be excluded here since high currents are transmitted through the film at rather low electric field. Other possibilities involve dispersive transport, observed in the band tails of amorphous Si,[38] nearest neighbor-[39] and variable range hopping.[40] The titania films that have been prepared on Si, GaAs and GaP are amorphous and a typical density of states (DOS) schematic is shown in Fig. 6.

One sees that, besides extended band tails, levels with higher DOS levels exist within the mobility gap. They have been attributed to defects with particularly high concentration. For nearest neighbor hopping, the conductivity, σ, depends on the concentration of nearest localization sites available, determined by the carrier localization length α, the defect concentration, N_0, and the concentration independent parameter σ_0 (10^2 - 10^4 $\Omega^{-1}cm^{-1}$) and $\gamma \sim 1.7$ is an empirical value in amorphous materials,[63] yielding a current, $j = \sigma E$, with:

$$\sigma = \sigma_0\exp\left[-\frac{\gamma}{\propto N_0^{\frac{1}{3}}}\right] \quad [11]$$

In amorphous Si solar cells, the use of p-i-n structures allows favorable competition of drift currents over diffusion where recombination dominates the transport. The drift, however, is due to transport at the mobility edges—energies of transition from localized to delocalized states—and results in high photocurrents. Carrier motion along lower lying levels is less effective and the question of the nature of the conductivity band in titania has not yet been resolved. What has not been considered in the above models is the incorporation of Ni into the amorphous TiO_2 film that can drastically alter the conductivity.[33] Defect analyses such as, for example, Brewster Angle Spectroscopy[41,42] could provide valuable insights. Variable range hopping occurs at lower temperatures and is not considered here further.

Case Studies: Surface Transformations

Early work.— The work on surface transformations for photoelectrode stabilization was initiated in the team of Adam Heller at Bell Laboratories, following work on ion adsorption that resulted in pronounced efficiency increases in GaAs photoanodes.[17,43] Within a short period, the first stable photocathode based on InP was communicated, showing a solar conversion efficiency of 9.4%, illuminated by natural sunlight of 110mWcm^{-2}[20] and cathodically stable Si.[44] In both cases, the presence of an interfacial film was postulated that allowed minority electron tunneling (Fig. 5a) while protecting against corrosion. The corresponding text is cited here verbatim: "*the formation of a very thin oxide layer on the surface of the p-InP electrode is likely upon either exposure to air or reaction with water*" and, in the case of Si: " *a thicker (SiO_2) film forms . . . near open circuit. . . however, even on long operation . . . near the maximum power point, the thickening of the SiO_2 layer is extremely slow and approaches a steady-state value.*"

Fig. 7 shows the combined output as a replica from this early work. The formation of an oxide film on InP on air was later confirmed.[21] The considerable differences in the photovoltage at relatively similar light intensity can be attributed to the alignment of the semiconductor Fermi level with the $V^{2+/3+}$ redox couple; whereas the Fermi level for p-Si is located near the potential of the saturated calomel electrode (vacuum work function ∼ 4.9 eV assuming 4.6 eV for the work function of SHE) and with −0.47V (SCE) for the redox potential of the vanadium couple, the contact potential difference (CPD) is ∼ 0.5V. In Fig. 7, the photovoltage is 0.4V demonstrating the validity of the energy alignment consideration. The S-shaped current onset from open circuit to more cathodic potentials indicates surface recombination and, possibly, also a series resistance problem due to an unoptimized thickness of the silicon oxide layer. This supposition is supported by the rather low short circuit current that should be considerably higher. The cell was, however, stable for 120 hrs operation at a load of 10Ω with an efficiency of 2.8%.

For p-InP, the electron affinity of the (111) A face that exposes In atoms, located $\frac{1}{4}$ atomic layer above the next row of P atoms, is 4.4 eV. With an energy gap of 1.35 eV and the Fermi level position, inferred from the doping level, 0.2 eV above the valence band edge, the CPD is obtained as E_{Redox} - E_F (InP) = E_{Redox} - [χ(InP) + E_g (InP) - (E_F-E_{VB})] = 4.4 eV - (4.4 eV+1.35 eV-0.2 eV) ∼ 1.1eV; however, uncertainties regarding the potential drop across interfacial layers have not been included. We find that, instead of a photovoltage of 1.1 V which is close to the Shockley-Queisser limit,[45] a value slightly below 0.7 V is observed. The behavior of the photocurrent between short circuit and the maximum power point (mpp) indicates shunt resistance losses that translate to non-negligible surface/interface recombination and indicate that the electronic properties at the InP-film interface are not fully optimized. Later, an efficiency increase via a modified surface treatment procedure[46] that includes . . . "*formation of a thin*

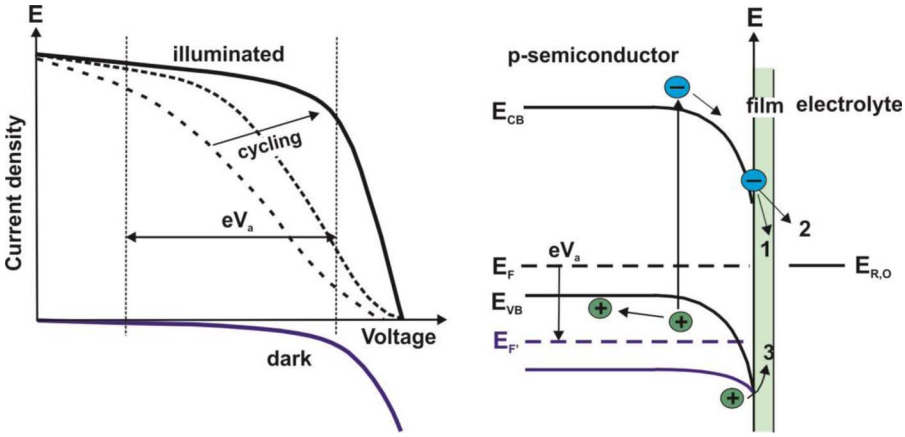

Figure 8. Current-voltage characteristic for semiconductor surface transformation and energy band schematic that translates the potential scan (eV_a, left image) into an energy scale (right); the dashed lines indicate the electrode performance before the cycling procedure; typically, a fill factor and open circuit voltage increase is observed if the potential limits, scan rate, light intensity and solution composition are chosen appropriately; black full lines: situation under illumination where cathodic reactions 1, 2 dominate; 1: reducing oxidized parts of interfacial film; 2: redox reaction; blue full lines: anodic dark current where majority holes oxidize the semiconductor (reaction labeled 3) (see text).

interfacial layer of a strongly chemisorbed species (which) substantially alleviates surface state related problems". . . to 11.5% was achieved.

An interfacial film formed upon exposure to air and/or water also was instrumental in the development of the first efficient water photolysis half cell.[47] Here, too, p-InP photocathodes were used as absorber and noble metal catalysts have been deposited onto the semiconductor surface. The solar-to-hydrogen conversion efficiency was 12%. Heller and co-workers note that the cell showed output issues where under continuous hydrogen evolution a performance decline was seen. On air or near the open circuit potential, the performance can be restored, which was attributed to reforming of a thin interfacial oxide-type film. Output data will be displayed below where hydrogen evolving systems are summarized.

The p-Si system (Fig. 7) suffered from (i) low efficiency and (ii) reduced stability. A pronounced improvement was achieved by the first publication of cycling an electrode within given potential limits.[48] The periodic cyclic polarization was done under illumination in the $V^{2+/3+}$ - HCl redox electrolyte with the applied voltage V_a varying as $+0.15\ V < V_a < +0.35\ V$ (SCE), i.e. between potentials anodic from the short circuit condition and cathodic from the open circuit which was at $+0.06V$ ($V_{ph} + 0.53$ V). A pronounced improvement of the output characteristics and simultaneous stabilization has been obtained and no significant hysteresis of the photocurrent existed upon cycling to V_{oc}. It will become clear in applications presented below that this processing sequence has considerable advantages and results in superior electrode performance. In a deaerated solution, such as the vanadium redox electrolyte that was N_2 purged, the coexistence of anodic forward and cathodic light-induced currents can be used to oxidize the surface via majority holes from the valence band while reduction processes can occur via the conduction band minority electrons as shown in Fig. 8.

The cyclic procedure is supposed to generate an interfacial film that is compact and stable when the electrode is operated as photocathode. A detailed mechanism describing how the interfacial film is stabilized by the scanning procedure has not yet been developed; such work necessitates *operando* experiments such as ambient pressure synchrotron photoelectron spectroscopy with tender X-rays for appropriate depth information which are presently performed at the Advanced Light Source.[49]

Revisiting InP photoelectrodes.— The work on interfacial film formation on InP was re-examined at the Hahn-Meitner Institute where the Department of Interfaces operated an Integrated Preparation-UHV Surface Analysis System that enabled investigation of samples, prepared and processed in various preparation chambers, without contact to ambient and, mostly, with direct transfer of the samples into a UHV transport mechanism system that connected to the surface analysis chamber. One end station provided the possibility for combined photoelectrochemistry-UHV photoelectron spectroscopy experiments. Later, a Solid-Liquid-Analysis System (SoLIAS) was installed at the undulator beamline U49–2 at the synchrotron BESSY II. Fig. 9 shows a photograph of the end station there where the attached glass vessel for photoelectrochemical conditioning under protective atmosphere is done. The samples are mounted on a vacuum stub that enables transfer from the electrochemistry chamber to a buffer chamber for outgassing after wet processing and further transfer into the UHV analysis chamber. (Photo)electrochemistry is done in an electrolyte formed by a droplets from the supply solution (shown on the lower left side of the SoLiAS photograph); as counter electrode (CE), a cylindrical Pt is used and the potential reference is a calomel electrode in contact with the droplet via a Luggin capillary. The rod that holds the CE also serves as light guide, allowing direct illumination of the electrode from above. After recording (photo)current-voltage characteristics or after chronoamperometric experiments, the electrolyte is removed by N_2 jet blowing and subsequently rinsed with de-aerated high purity water, followed by drying in 5N nitrogen stream. The sample is then transferred to a buffer chamber and, if the pressure reaches 10^{-9} hp, transfer into the UHV analysis chamber is made. This procedure, where the sample is inserted into the glass reaction vessel from the machine side and left there for approximately a day before processing, results in ultralow contamination levels for samples where electrochemical currents have passed; a typical contamination with hydrocarbons is in the range of 0.1atomic layers (ML), thus allowing the application of all UHV analysis techniques, including LEED, UPS, HREELS, SRXPS (synchrotron radiation XPS), AES, for example. This *in-system* analysis method, however, will only detect surface species that are strongly enough bound to the surface to withstand the rinsing and drying procedure and, in this respect, it is less sensitive for intermediates than present day's *operando* XPS. Because of the demand to maintain an ultrathin electrolyte film on the surface for *operando* measurements, the tender X-rays (2–6 keV) are typically used as probe light since their inelastic scattering length of photoelectrons is in the 10—30 nm range. Fig. 10 shows a photograph of the respective experiment at the beamline 9.3.1 at the Advanced Light Source (ALS) at LBNL.

Because of the rather large inelastic scattering length for photoelectrons with higher kinetic energy, one samples the solid surface, the interfacial electrolyte layer (inner and outer Helmholtz layer), adjacent water and water vapor. Due to the integral measurements over several 10 atomic layers, the sensitivity for a particular interface is lower than in the *in-system* UHV experiments despite the possibility to alter the photon energy within a certain range, adjusting the depth resolution between ~10 nm and 30 nm. This, however, is compensated by the rather facile way of recording interfacial reactions via core level spectroscopy in APXPS.

The analysis of the interfacial conditions on photoelectrochemically conditioned InP photocathodes commenced with an adaption of the traditional treatments. Fig. 11 shows that upon repeated cycling in HCl under white light illumination, a pronounced fill factor and photovoltage increase is observed.

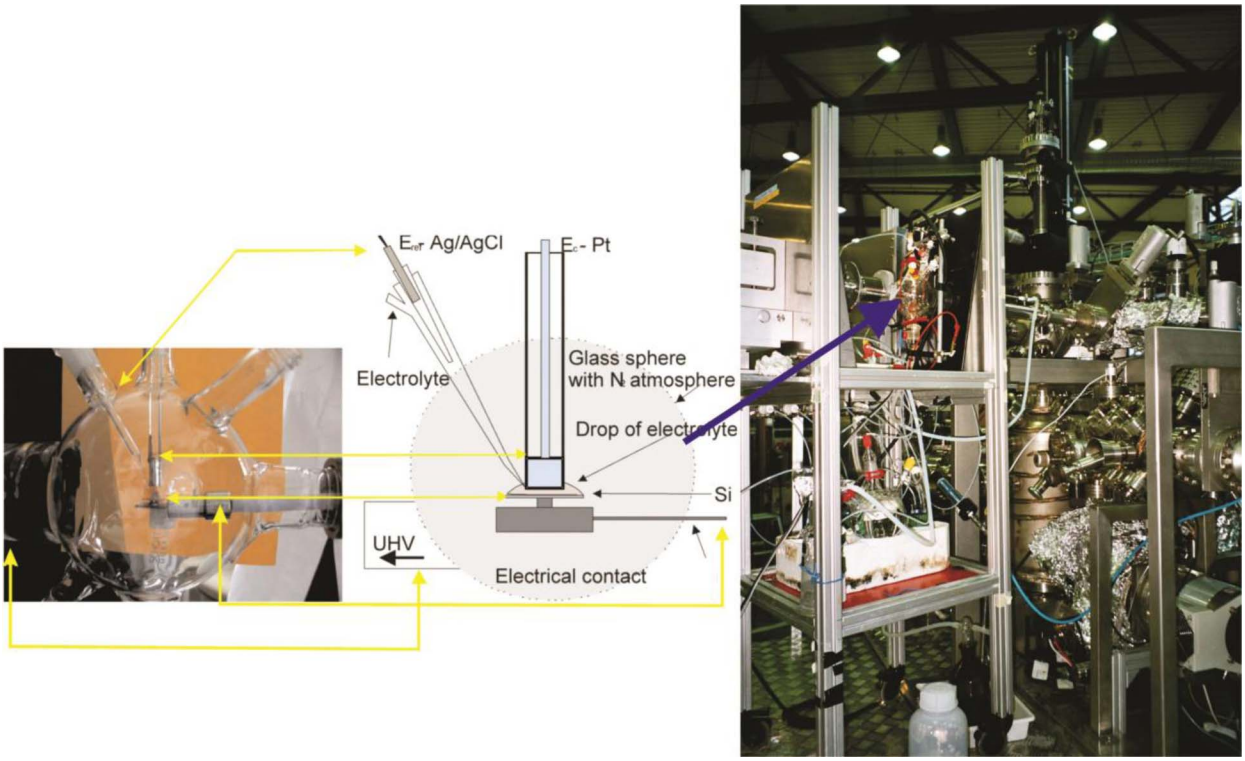

Figure 9. Combined (photo)electrochemistry-surface analysis system attached to the SoLiAS end station at the undulator U49/2 at BESSY II; the arrow shows the electrochemical processing chamber; the left part of the figure shows details of the processing chamber (see text).

The conditioning procedure resulted in a 11.6% efficient photoelectrochemical solar cell, measured at 55 mWcm^{-2} in natural sunlight in a two-electrode arrangement.[50] Making use of the improved analytical capabilities (Fig. 9), the chemical nature of the interfacial film and the electronic situation at the InP/film/electrolyte contact can be assessed.[51] One finds that after the optimization in HCl, a film has formed on the surface of InP that consists of In_2O_3, InCl and Indium phosphate group to a lesser extent. The P signal is not displayed in Fig. 12: the low binding energy and the resulting large kinetic energy and large sampling depth and the fact that P is the major constituent of InP does not allow to assess surface changes. The film thickness, determined from the standard evaluation using the exponential decay of the photoemission signal that is determined by the mean inelastic scattering length for the respective core levels results in a thickness of an interfacial film of ~ 0.7 nm after optimization in the vanadium electrolyte. One finds that the film thickness by conditioning in HCl is larger and amounts to about 1 nm.

The formation of surface species can be inferred from the corrosion products in chloride containing solution upon anodization of the sample where the holes h^+ originate from the valence band or from surface states

$$p - InP + 6h^+_{VB,SS} + nH_2O + Cl \Rightarrow In^{3+}(H_2O)_{n-y}Cl + PO_y^{3-y} + 2yH^+_{aq} \quad [12]$$

The reduction reaction is

$$p - InP + 3e^-_{CB}(h\nu) + 3H^+_{aq} \Rightarrow In^0 + PH_3 \quad [13]$$

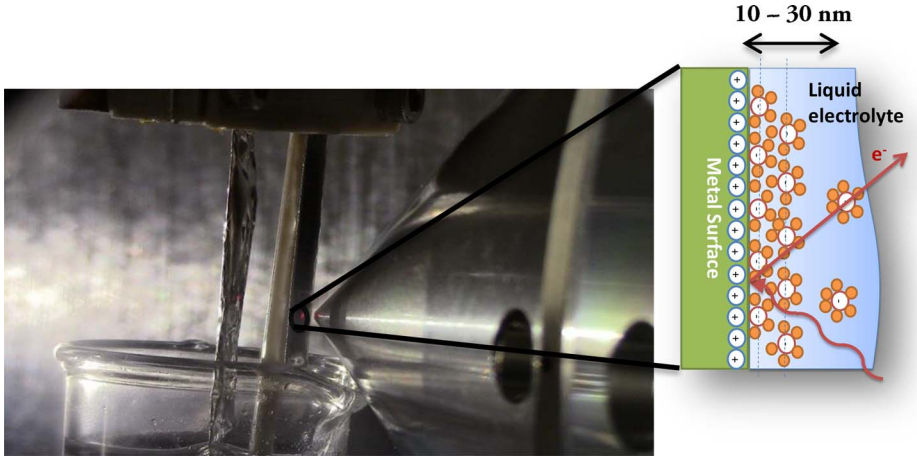

Figure 10. Experimental arrangement for ambient pressure photoelectron spectroscopy at the ALS (left) and surface sensitivity in the tender X-ray experiment (see text).

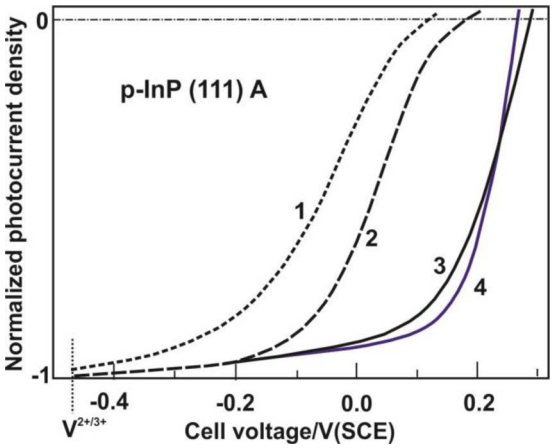

Figure 11. Photocurrent-voltage characteristics of p-InP in 0.5 M HCl (curves 1–3) and in $V^{2+/3+}$ redox electrolyte (curve 4); curve 1: untreated electrode; curve 2: after etching in 1% Br_2-CH_3OH for 30 s; curve 3: after 50 cycles in HCl, $-0.6\ V < V_a < +0.2$ V, scan rate 20 mVs^{-1}; curve 4: after 5–10 cycles in $V^{2+/3+}$ - 4MHCl redox electrolyte; also indicated is the redox potential of −0.47 V.

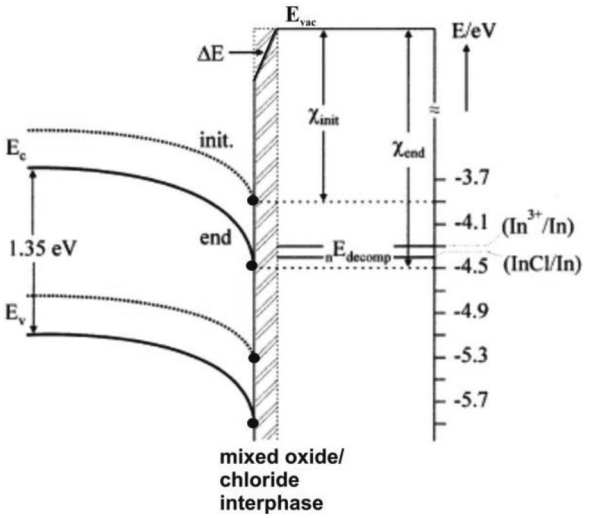

Figure 13. Energy band relations induced by the in-situ conditioning procedures; the condition labeled 'init.' refers to the situation before the cycling in HCl, 'end' denotes optimization according to curve 3 in Fig. 11; also indicated are decomposition potentials $_nE_{dec}$, related to In metal formation.

but, obviously, the conditioning procedure does not result in the formation of In metal, likely because the anodization will result in indium oxide, -chloride and -phosphates even if In^0 would be formed in the cathodic branch of the scanning procedure.

The alteration of the energy relations due to the conditioning procedure can be analyzed by UPS, where the spectral width, the difference between Fermi level position and valence band emission and the secondary electron cut-off allow to determine semiconductor band bending (and its changes) and the electron affinity. The data show that the electron affinity determined from the expression $\chi = h\nu - E_g - S_W$ where $h\nu$, E_g and S_W are the photon energy (21,2 eV), the energy gap (1.25 eV for InP) and the spectral width which is determined as the difference of the secondary electron cut-off and the onset of the valence band emission. It is found that the surface transformation that leads to the interfacial film is also accompanied by a change in the electronic alignment of the energy levels such as the conduction and valence band edge positions with respect to the decomposition energy levels. The result is shown as an energy schematic in Fig. 13.

It turns out that the conditioning process resulted in the formation of an interfacial film of tunneling thickness and that the conduction band edge position is shifted downwards by about 0.5 eV compared to the starting situation. A stable condition is reached when the cycling process yields an interphase where the decomposition levels are energetically located above the conduction band edge where electrons are injected into solution. In $V^{2+/3+}$ electrolyte, the final few cycles result in a thinner film and a lower electron affinity. The film formed in the vanadium redox solution, however, is compact, corrosion is inhibited and the band edge position is not important anymore.

Although the surface chemistry of compound semiconductors exposed to various electrolytes und various conditions can be highly complex as seen from the XPS data, judicious choice of parameters and processing conditions can result in fabrication of corrosion protection layers while stabilizing the cell. Below, two additional approaches for the advantageous use of corrosion products will be presented.

Nanoemitter solar cells.— The nanoemitter (NE) concept originates from the observation of oscillating (photo)currents of Si in fluoride containing electrolytes.[52–54] It was found that, upon precise control of the solution composition including the pH, sustained oscillations could be observed that are related to the etch rate of SiO_2 that is formed as corrosion product at the anodic potentials V_a were

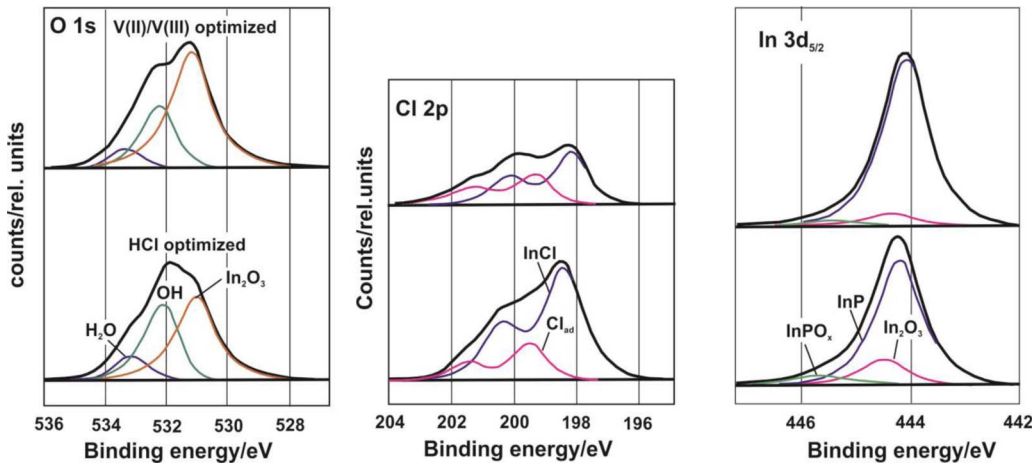

Figure 12. In-system XPS analysis of the surface chemistry of p-InP after optimization of the output power characteristic in HCl (curve 3 in Fig. 11) and after further optimization of the performance in $V^{2+/3+}$ redox electrolyte (curve 4 in Fig. 11), upper part of the signals in the figure; XPS source: Mg K_α ($h\nu = 1256$ eV).

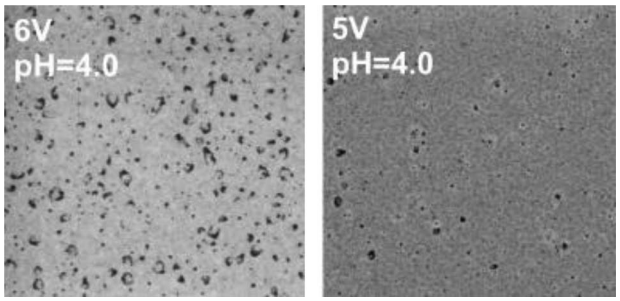

Figure 14. HRSEM image of nanoporous silicon oxide formed by sustained photocurrent oscillations; electrolyte: 0.1M NH_4F; image size 3×3 μm (see text).

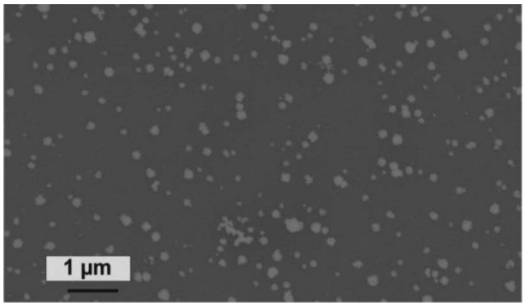

Figure 16. HRSEM image of Pt-nanoporous oxide-Si structure after ED form $PtCl_6^{2-}$ (see text).

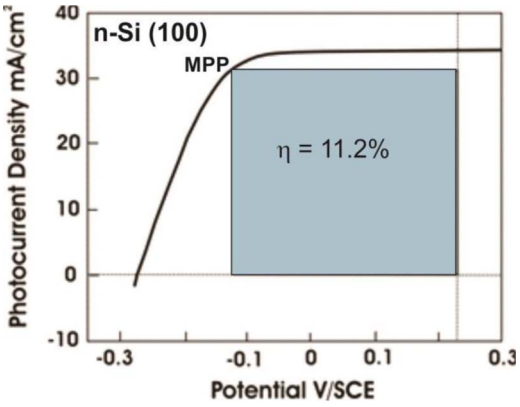

Figure 17. Photocurrent-voltage curve for an n-Si nanoemitter cell with Pt as emitter material (see text).

the phenomenon is present. The period of the oscillations can be adjusted by the parameters that influence the silicon oxide etch rate, e.g. [HF], [HF_2^-], [H^+] and [F^-]. Besides the development of a theoretical description that is based on a combination of probability theory and Markov processes,[55] and employing cellular automata for spatial resolution,[56] investigations on the formed interphase were performed. *Operando* FTIR experiments[57] showed a periodic (integral) thickness (d_f) variation of the oxide film with 8 nm < d_f < 11 nm, with d_f depending on the respective conditions (k_e, V_a light intensity). The photocurrent on n-type samples, however, was also strongly modulated which was unexpected because at thicknesses beyond 2 nm (tunneling thickness), currents should cede. This led to the postulate that the formed anodic oxide film is porous and, since larger pores were not visible in optical analyses, nanopore formation had been inferred. Such pores were indeed observed in HRSEM experiments and Fig. 14 shows an array. In this case, the electrode potential is shown to have a significant influence on the pore patterns; at +6 V (SC E), the pore density is considerably higher and the sizes differ.

The current transport obviously occurred through these pores in the oscillation experiments. The pore size, distribution and density also change during an oscillatory cycle and the areas without pores (d_f ~10 nm) were considered to be insulating.

The step toward application was to make use of the nanoporosity by formation of local contacts between the Si substrate and the electrolyte. The concept is shown in Fig. 15 where the size of the conducting contacts, the space charge region around them, the minority carrier diffusion length and the condition for optimized current collection are given for a mostly lateral system and for a structure with deepened pores that would increase the red sensitivity of the solar cell.

Although also applicable for solid-state solar cells, the first realization was the preparation of a photovoltaic electrochemical solar cell. The cell was prepared by electrodeposition of Pt from a hexachloro complex site-selectively into the nanopores, as shown in Fig. 16; one sees that the Pt islands are distributed in a highly localized manner.

In first experiments on the photoelectrochemical behavior of n-Si NE cells, the quality of the electrical contact between electrolyte and the Si substrate was found to influence the performance; accordingly, an alkaline etching procedure was developed that enhanced the contact between the NE material (Pt) and Si. As a result, efficient solar energy conversion was obtained in acidic I^-/I_3^- electrolyte (see Fig. 17). It should be mentioned that the stability of the cell shown in Fig. 17 is limited because of the bonding of I to Pt. The cell output had to be recovered by cycling to cathodic potentials where H_2 evolution occurs via the majority carriers.

A somewhat different procedure was employed to fabricate a photocathode for light-induced water splitting: H-terminated p-type Si

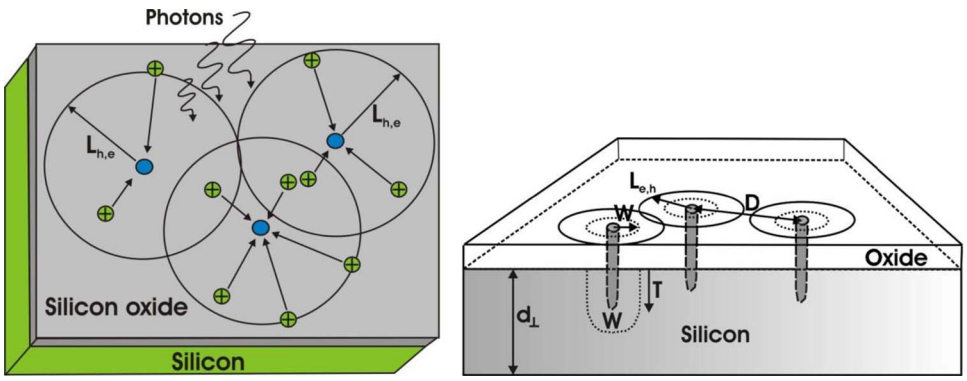

Figure 15. Concept of nanoemitter solar cells that consist of a nanoporous passivating layer on top of a light absorber; conditions for lateral and vertical optimization are given; L: minority carrier diffusion length, blue circles: space charge region and diameter of the nanoemitter spots; for complete overlap of the charge collection sphere, the inequality $D < 2^{0.5}[L + W + r_{NE}]$ has to be fulfilled; D: distance between NEs, W: space charge region, r_{NE}: NE radius; for increased red sensitivity the condition reads: T = D - [W - L/2] (see text).

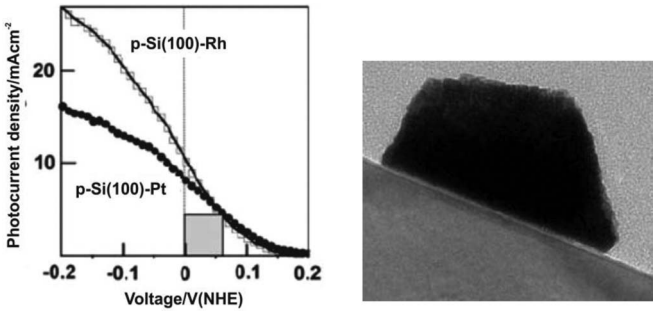

Figure 18. Photocurrent-voltage characteristic of a p-Si/Pt nanoemitter cell in H_2SO_4, illuminated by white light (W-I lamp) at 100 $mWcm^{-2}$; Pt, Rh nanoparticles prepared by electrodeposition onto former H-terminated surfaces; on the right hand side: TEM cross-sectional image of a Pt island after ED onto Si substrate; note the thin interfacial film; the island is about 100 nm wide.

was used as substrate for photoelectrodeposition of Pt and Rh nanoparticles. The photoelectrodeposition process is accompanied by the formation of a thin interfacial oxide film due to hole injection into the valence band and into surface states. In the presence of water, this results in oxidation of Si via solvolytic splitting of backbonds. The performance was limited because of the low CPD between the Fermi level of p-Si and the H^+/H_2 redox couple. Here, however, stability was not an issue and Fig. 18 shows an output power characteristic. With a short circuit current density of 34 $mAcm^{-2}$, an open circuit voltage of 0.5 V and a fill factor of 0.65 at a light intensity of 100 $mWcm^{-2}$ (W-I lamp), the given solar-to-electricity efficiency results.

The nanoemitter concept has several rather striking advantages: (i) processing occurs at ambient temperature and is scalable, (ii) photovoltaic as well as photoelectrocatalytic systems with high efficiency can be prepared with low light shadowing effects, (iii) photoelectrochemical and solid state devices can be prepared, (iv) materials with low carrier mobility can be optimized by altering the distance between the emitter spots, (v) the vertical structure allows efficient collection in low absorption materials.

InP photocathodes.— As mentioned in previously the output characteristics of the first efficient hydrogen evolving half cell by Heller and Vadimsky[47] are presented in Fig. 19. In this case, an anisotropic etching has been employed where uncovered parts of the semiconductor were etched away but electrocatalyst covered areas remained, except for certain undercutting. The protection layer was formed by oxidation of InP by dilute aqua regia, extended immersion into 1M HCl and exposure to an oxygen stream. The solar-to-hydrogen efficiency, calculated using the shown rectangle, reaches 12% and this

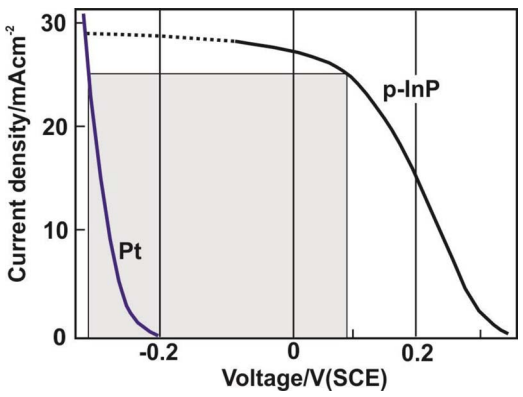

Figure 19. Output power characteristic of a Pt/Rh/film/InP photocathode in HCl-KCl electrolyte; illumination 84.7 $mWcm^{-2}$ (natural sunlight); the Pt anode was covered by electroplated Rh.

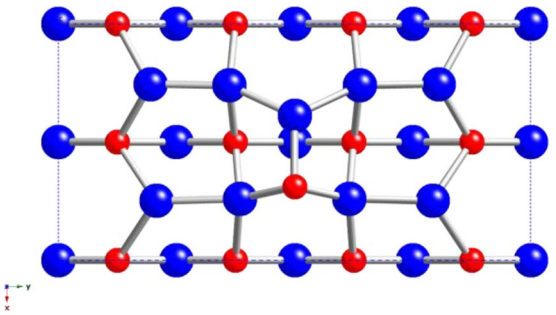

Figure 20. Surface atom arrangement of the (2 × 4):(100) InP surface; blue spheres: In atoms, red: P atoms.

result presented the first breakthrough in efficient solar hydrogen generation.

Single crystalline InP is a rather expensive material and a material saving alternative is provided using thin homoepitaxial films with reusable InP substrates. InP homoepitaxial layers have been prepared by $MOCVD^{cit}$ on InP substrates, custom - made for applications in photoelectrochemistry where ∼ 3 μm thick absorbers are needed. Based on the experience with InP from the Bell Laboratories group where (111) A faces were used that exhibit a specific surface chemistry, here, too, an In-rich surface has been prepared. Instead of a (111) surface, a (2×4) reconstructed (100) surface, where the top surface layer consists of 8 In atoms and 1 P atom as can be seen in Fig. 20.

The doping level (Zn doping for p-type conductivity) was adjusted to be in the mid $10^{17}cm^{-3}$ range. The work on the new layers was aimed at developing a high-efficiency stable thin film hydrogen evolving half cell that can then be implemented into a tandem structure with anode and cathode protection layers for unassisted light-induced water splitting. Based on the experience with electricity generating InP cells, a modified conditioning procedure for interfacial protective film formation has been employed. The films as obtained from the MOCVD growth showed very low photoactivity and, for photoactivation, a scanning procedure in 1M HCl was used; the electrode potential was cycled under illumination between −0.1V and +0.3 V (SCE) and after 50 cycles the photocurrent improved from 300 μAcm^{-2} to 4.8 $mAcm^{-2}$. It was presumed from the corrosion reactions shown below that the procedure altered the surface layer in a way that high photoactivity resulted.

$$2In + 6h^+(VB, SS) + 3H_2O \rightarrow In_2O_3 + 6H^+_{aq}$$

$$3InP + 15H_2O + 24h^+(VB, SS) \rightarrow In(PO_3)_3$$

$$+2In(OH)_3 + 24H^+_{aq}$$

$$InP + 4H_2O + 8h^+(VB, SS) \rightarrow In(PO_4) + 8H^+_{aq} \quad [14]$$

Rh photoelectrodeposition was made at −0.2 V (SCE) for 4 min.; the chronoamperometric deposition profile was monitored until a distinct current decay indicated saturation. The structure Rh/interphase/p-InP (100):(2×4)/InP substrate was immersed into 1M $HClO_4$ and cycled for further optimization which resulted in a solar-to-hydrogen efficiency of 14.5% if the efficiency determination from Ref. 47 is used[31] and of $\eta = 12.4\%$ if one takes the potential of the hydrogen redox couple as reference. The output characteristics are displayed in Fig. 21.

The cell showed very high stability as evidenced by a series of cross-sectional TEM images where the interface between the film and the InP absorber was completely unaffected after currents passed that would have resulted in 14μm material's loss as shown in Fig. 22.

The interphase found here is too thick for tunneling but not porous as in the case of the anodic oxide formed during oscillations at Si. For chemical analysis and energy band relation assessment, synchrotron radiation photoelectron spectroscopy (SRPES) was performed. The method allows tuning of the photon energy such that for each core

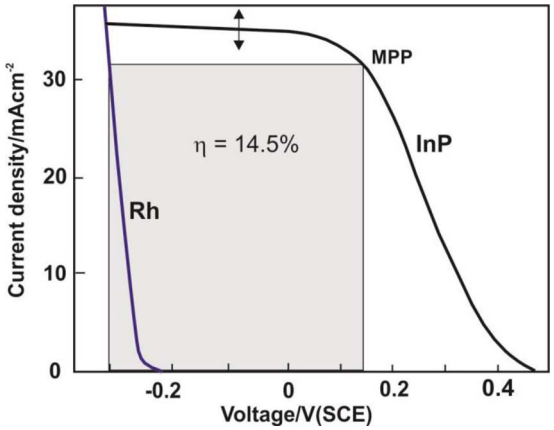

Figure 21. Output characteristics of the Rh/film/p-InP/$HClO_4$/C cell; illumination 105 mWcm^{-2} (W-I lamp), electrolyte 1 M $HClO_4$, the arrow indicates the current fluctuation due to hydrogen bubble formation (see text).

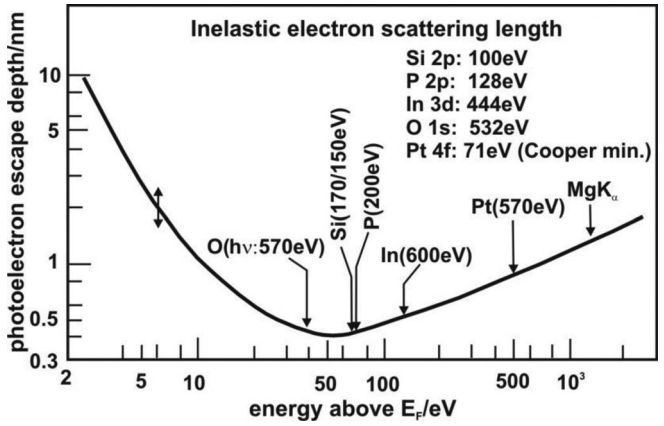

Figure 23. Mean inelastic scattering length, □λ_f, of photoelectrons with indication of some of the relevant elements (Si, O, P, In); also shown is the Pt 4f core level energy and the □λ_f value for electrons excited from the Fermi level with MgKα□ radiation.

level, maximum surface sensitivity can be achieved. In laboratory XPS, the fixed photon energy results in different photoelectron escape depths, depending on the kinetic energy which is given by the energetic position of the respective core levels. Fig. 23 shows the mean inelastic scattering length for photoelectrons and the corresponding core levels; note that here, the P 1s line can be evaluated with high surface sensitivity. The evaluation of the SRPES data in combination with AFM and TEM and the corrosion reactions yielded the following picture of the device structure after optimization in the cycling procedure, i.e. without the Rh catalysts:

It is obvious that the interphase has a composition distribution with thickness where the indium oxide component decreases toward the outer surface, the phosphate component has a maximum toward the middle of the film and the $(PO_3)_3$ component shows an increase at the surface (Fig. 24). This indicates formation of an about 7–10 nm thick indium oxide film with indium phosphate components. Chloride related signals as in the case of the InP (111) A face were not detected here. The electronic situation has been determined using UPS and valence band XPS (VB-XPS); Fig. 25 shows the situation before contact and after contact formation.

The energy relations in Fig. 25 show that, obviously, the cycling procedure in HCl has initiated the growth of a thicker indium oxide/phosphate film that is n-type doped by the formation method. Hence, an internal n-p junction forms between this film and the p-InP absorber. The optical gap is large (∼3 eV) and this phase does not absorb significant light. The electron affinity of the interphase is such that thermalized excess minority carriers from InP can be transported along the interphase conduction band. Accordingly, this film allows for excellent conduction while simultaneously blocking access of electrolyte to the absorber surface which results in the exceptional stability.

The highly textured Rh catalysts show optical properties that make the material rather transparent in the wavelength range where absorption in InP occurs. The photocurrent-voltage behavior of such a catalyst covered photodiode, immersed into a solution, has recently been modeled[58] and the output characteristics could be reproduced with high accuracy; the potential-current relationship is given below for a diode:

$$V_{diode}(j) = \frac{n_d kT}{q} \ln\left(\frac{j_L - j}{j_{0,PV}} + 1\right) - \frac{2RT}{n_e F} \sinh^{-1}\left(\frac{j}{2j_{0,cat}}\right) \quad [15]$$

Here, the first term describes the photoactivity of the solid state part of the device and the second term its electrochemical behavior; j_L denotes the light-induced current, j the operating current, $j_{0,PV}$ is the reverse saturation current and n_d is the junction ideality factor. In the second term, $j_{0,cat}$ is the exchange current density of the catalyst and n_e the number of electrons transferred in the reaction. Expression (15) can be extended to include the absorption of the electrocatalyst and the surface area enhancement compared to the geometric surface that is clearly visible in Fig. 22. The advanced equation then reads:[59]

$$V_{diode}(j) = \frac{n_d kT}{q} \ln\left(\frac{j_L f_T - j}{j_{0,PV}} + 1\right) - \frac{2RT}{n_e F} \sinh^{-1}\left(\frac{j}{2j_{0,cat} f_{SA}}\right) \quad [16]$$

The new terms, f_T and f_{SA} include factors that modulate the light-induced current and the exchange current. The former is a transmission factor that accounts for non-unity transmission of the incoming

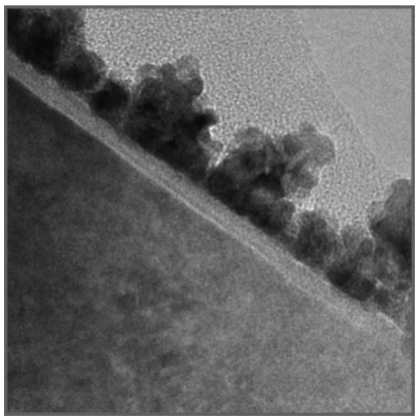

Figure 22. TEM image of the Rh/film/InP structure after passage of 45 Ccm^{-2}; the film is about 7 nm thick (see text).

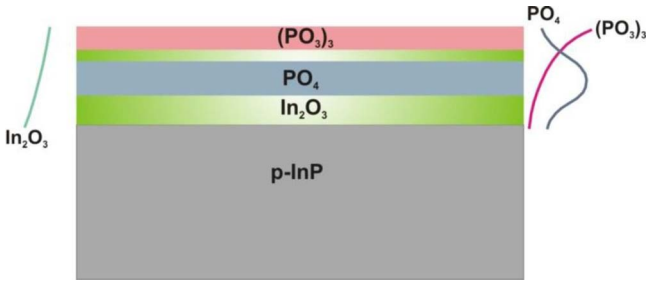

Figure 24. Schematic of the layer structure after photoelectrochemical conditioning of the InP thin film absorber; the profiles at the left and right hand side describe the signal intensity and show that the surface phase formed changes its composition (see text).

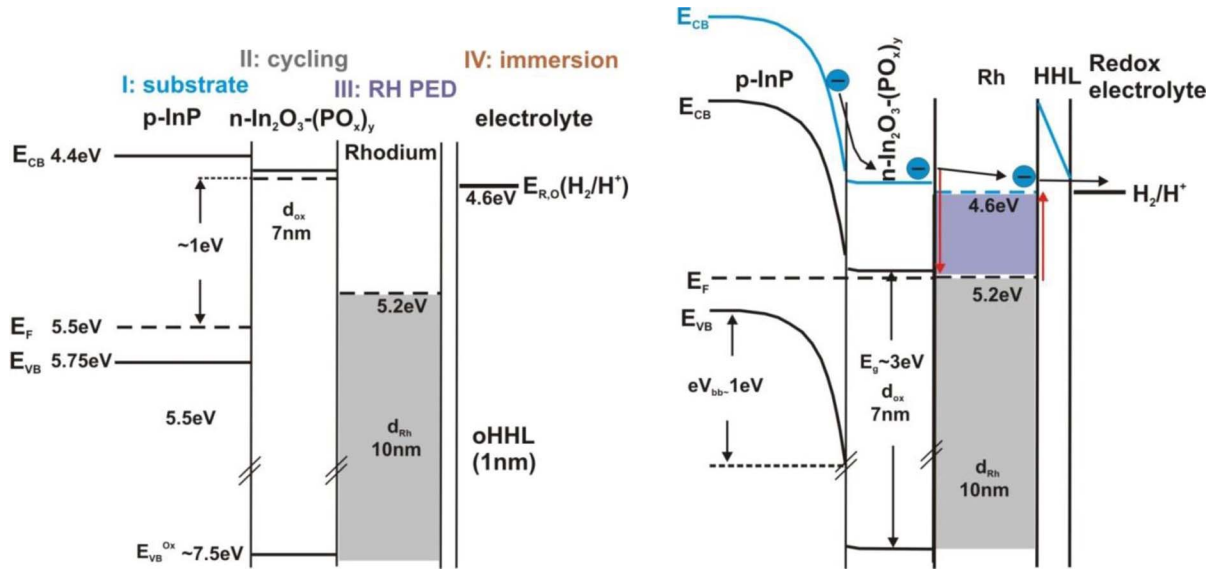

Figure 25. Energetic situation of the Rh/film/InP/electrolyte hydrogen evolving half cell; left: before contact, right: after contact formation; red arrows indicate (i) band edge shift of the interfacial film and (ii) Fermi level shift of Rh upon contact with the redox electrolyte (see text).

light to the absorber surface and the latter takes the presence of a nanostructured electrocatalyst layer into account whose surface area distinctively deviates from that of a planar surface. Thus, the catalytic exchange current density can be normalized. Fig. 26 shows the modeling of the output power characteristics of Fig. 21 based already on eqn. 15 and inserting a series resistance.

Recently, a similar method has been applied to optimize a highly efficient tandem structure that is able to split water upon illumination with an efficiency that exceeds 13% at one sun;[60] the surface conditioning procedure is intricate and first result will be made available soon.

Synopsis

This article focuses on one of the important innovations that Adam Heller introduced into photoelectrochemistry and, in particular, in photoelectrochemical energy conversion: the *operando* or in-situ preparation of corrosion protection layers that, simultaneously, have electronic properties that maintain or improve the performance of the light absorber. I have shown that, particularly in the light of the renewed interest in photoelectrochemistry for solar energy generation, this approach is still very valuable and is pursued until today with sometimes exceptional results. An important aspect of the in-situ conditioning was always its conformity to the absorber surface which, however, is natural for electrochemical processes. Meanwhile, another conformal method, atomic layer deposition has shown its strength in stabilizing photoanodes. This opens new avenues to the realization of stable and efficient systems in the development horizon for artificial leaves. However, the interfacial chemistry of the in-situ conditioning method and of ALD processes is intricate. I envisage that the complex chemistry of these compound material interfaces, will keep us busy for an extended period of time, even with the help of theory and advanced characterization tools. Presently, the search has begun for a different type of artificial leaf, i.e. one that produces oxygen and, simultaneously reduces carbon dioxide. These processes involve transfer of altogether 10–12 electrons (if the products are methanol or methane) that is coupled to proton transfer. This endeavor will stimulate further research on proton coupled electron transfer in the sequential and concerted mode which will need advanced dynamical analyses. So, our work goes on, and is very exciting. The following is a statement that Adam Heller once made to me, with which I close this article: "*Introspection is like good science, it never ends*".

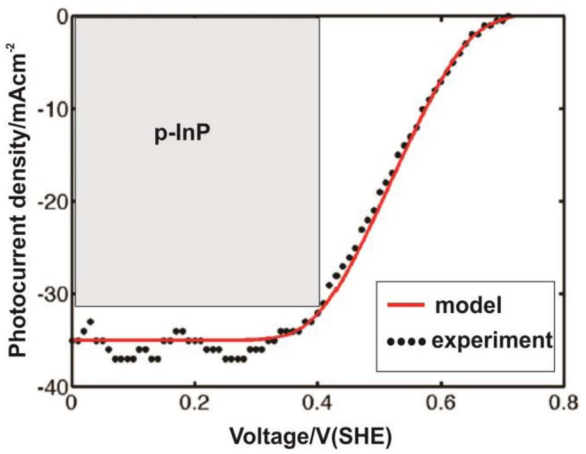

Figure 26. Modeling of the output power characteristics of the p-InP/n-indium oxide/phosphate film/Rh cell (Fig. 21); (see text).

Acknowledgment

The author is indebted to the Bell Laboratories team led by Adam Heller, which also included Barry Miller, Klaus Bachmann, Shalini Menezes, Ferdinand Thiel and Dave Aspnes; from the group at the Hahn-Meitner Institute in Berlin (now the Helmholtz Zentrum Berlin after merging with the synchrotron facility Bessy II), I acknowledge contributions of Mohammed Aggour, Juergen Grzanna, Thomas Stempel, Andres Munoz, Katarzyna Skorupska Christian Heine, Thomas Hannappel, Matthias May, Oliver Supplie and Ulrike Bloeck. At Caltech, enlightening discussions with Matthew Shaner, Katherine Fountaine and Harry Atwater are gratefully acknowledged. Part of the work described here was funded by the DFG (Project No. LE 1192–4). This material is based upon work performed by the Joint Center for Artificial Photosynthesis, a DOE Energy Innovation Hub, as follows: the composition and the writing of the review as well as the modeling results were supported through the Office of Science of the US Department of Energy under Award No. DE-SC00049993.

References

1. H. Gerischer, *J. Electroanal. Chem.* **58**, 263 (1975).
2. H. Gerischer in: *Semiconductor-Liquid Junction Solar Cells*, *The Electrochemical Soc., Proceedings* Vol. **77-3**, editor A. Heller, pp. 1-19 (1977).
3. A. Fujishima and K. Honda, *Nature* **238**, 37 (1972).

4. J. K. Sass and H. J. Lewerenz, *Journ. de Phys.* **38**(C5), 277 (1977).
5. H. J. Lewerenz, J. K. Sass, E. Piltz, and H. Neff, *Surf. Sci.* **80**, 141 (1979).
6. A. J. Nozik, *Ann. Rev. Phys. Chem.* **52**, 193 (2001).
7. G. Cooper, J. A. Turner, B. A. Parkinson, and A. J. Nozik, *Appl. Phys. Lett.* **54**, 6463 (1983).
8. M. Halmann, *Nature* **275**, 115 (1978).
9. I. Taniguchi, B. Aurian-Blajeni, and J. O'M. Bockris, *Electrochim. Acta* **29**, 923 (1984).
10. H. Gerischer, *J. Vac. Sci. Technol.* **15**, 1422 (1978).
11. B. Miller, S. Menezes, and A. Heller, *J. Electrochem. Soc.* **126**, 1483 (1979).
12. H. Gerischer, *J. Electroanal. Chem. Interfac. Electrochem.* **82**, 133 (1977).
13. J. Gobrecht, H. Gerischer, and H. Tribusch, *Ber. Bunsenges. Phys. Chem.* **82**, 1331 (1978).
14. H. J. Lewerenz, A. Heller, and F. J. DiSalvo, *J. Am. Chem. Soc.* **102**, 1877 (1980).
15. H. J. Lewerenz, H. Gerischer, and M. Luebke, *J. Electrochem. Soc.* **131**, 100 (1984).
16. S. Licht, G. Hodes, R. Tenne, and J. Manassen, *Nature* **326**, 863 (1987).
17. B. A. Parkinson, A. Heller, and B. Miller, *Appl. Phys. Lett.* **33**, 521 (1978).
18. K. W. Frese Jr., *Appl. Phys. Lett.* **40**, 275 (1982).
19. M. A. Butler and D. S. Ginley, *J. Mat. Sci.* **15**, 1 (1980).
20. A. Heller, B. Miller, H. J. Lewerenz, and K. J. Bachmann, *J. Am. Chem. Soc.* **102**, 6555 (1980).
21. H. J. Lewerenz, A. Heller, B. Miller, D. Malm, and D. E. Aspnes, *J. Am. Chem. Soc.* **104**, 3325 (1982).
22. W. Shockley: *Electrons and Holes in Semiconductors*, van Nostrand Publ. Comp., section 12.4, pp 302 ff (1950).
23. A. J. Bard and M. S. Wrighton, *J. Electrochem. Soc.* **124**, 1706 (1977).
24. W. M. Latimer: *Oxidation Potentials*, 2nd edition, Prentice Hall, New York (1952).
25. H. J. Lewerenz in: *Advances in Electrochemical Science and Engineering, chapter 2 in Vol. 12: Photoelectrochemical Materials and Energy Conversion Processes*, Eds. R. Alkire, D. M. Kolb, J. Lipkowski, and P. N. Ross, Wiley-VCH (2010).
26. R. A. Marcus, *Rev. Mod. Phys.* **65**, 599 (1993).
27. K. Skorupska, Ch. Pettenkofer, S. Sadewasser, F. Streicher, W. Haiss, and H. J. Lewerenz, *Phys. Stat. Sol. (b)* **248**, 361 (2011).
28. S. M. Sze and K. K. Ng: *Physics of Semiconductor Devices*, 3rd Ed., Wiley (2007).
29. S. M. George, *Chem. Rev.* **110**, 111 (2010).
30. S. Menezes, H. J. Lewerenz, and K. J. Bachmann, *Nature* **305**, 615 (1983).
31. H. J. Lewerenz, C. Heine, K. Skorupska, N. Szabo, T. Hannappel, T. Vo-Dinh, S. A. Campbell, H. W. Klemm, and A. G. Munoz, *Energy Environm. Sci.* **3**, 748 (2010).
32. W. W. Gaertner, *Phys. Rev.* **116**, 84 (1959).
33. S. Hu, M. R. Shaner, J. A. Beardslee, M. Lichterman, B. S. Brunschwig, and N. S. Lewis, *Science* **344**, 1005 (2014).
34. E. A. Davis and N. F. Mott, *Phil. Mag.* **22**, 903 (1970).
35. R. M. Hill, *Phil. Mag.* **23**, 59 (1971).
36. H. J. Lewerenz, K. Skorupska, J. R. Smith, and S. A. Campbell, *J. Sol. State. Electrochem.* **13**, 195 (2009).
37. S. K. Gupta, A. Azam, and J. Akhtar, *Pramana J. Phys.* **74**, 325 (2010).
38. T. Tiedje and A. Rose, *Sol. State Comm.* **37** 49 (1981).
39. H. Q. Lin and J. E. Hirsch, *Phys. Rev. B* **35**, 3359 (1987).
40. R. M. Hill, *Phys. Stat. Sol. (a)* **35**, K29 (1976).
41. H. J. Lewerenz and N. Dietz, *Appl. Phys. Lett.* **59**, 1470 (1991).
42. M. Lublow and H. J. Lewerenz, *Surf. Sci.* **602**, 1677 (2008).
43. A. Heller, H. J. Lewerenz, and B. Miller, *Ber. Bunsenges. Phys. Chem.* **84**, 592 (1980).
44. A. Heller, H. J. Lewerenz, and B. Miller, *J. Am. Chem. Soc.* **103**, 200 (1981).
45. W. Shockley and H. J. Queisser, *Appl. Phys. Lett.* **32**, 510 (1961).
46. A. Heller, B. Miller, and F. A. Thiel, *Appl. Phys. Lett.* **38**, 282 (1981).
47. A. Heller and R. G. Vadimsky, *Phys. Rev. Lett.* **46**, 1153 (1981).
48. H. J. Lewerenz, S. Menezes, M. Luebke, and K. J. Bachmann, *Appl. Phys. Lett.* **39**, 798 (1981).
49. M. Richter, M. Lichtermann, S. Hu, N. S. Lewis, and H. J. Lewerenz, manuscript in preparation.
50. K. Schulte and H. J. Lewerenz, *Electrochim. Acta* **47**, 2633 (2002).
51. H. J. Lewerenz and K. Schulte, *Electrochim. Acta* **47**, 2639 (2002).
52. H. J. Lewerenz and G. Schlichthoerl, *J. Electroanal. Chem.* **327** 85 (1992).
53. J.-N. Chazalviel, F. Ozanam, M. Etman, F. Paolucci, L. M. Peter, and J. Stumper, *J. Electrochem. Soc.* **327**, 343 (1992).
54. H. J. Lewerenz and M. Aggour, *J. Electroanal. Chem.* **351**, 159 (1993).
55. J. Grzanna, H. Jungblut, and H. J. Lewerenz, *J. Electroanal. Chem.* **486**, 181 (2000); *ibid.* p.190.
56. J. Grzanna, T. Notz, T. Stempel, and H.-J. Lewerenz, *Phys. status solidi C*, **8**, 1734 (2011).
57. J. Rappich, M. Aggour, H. J. Lewerenz, S. Rauscher, and H. Jungblut, *Surf. Sci.* **335**, 160 (1995).
58. M. Shaner, K. Fountaine, and H. J. Lewerenz, *Appl. Phys. Lett.* **103**, 143905 (2013).
59. K. T. Fountaine, H. J. Lewerenz, and H. A. Atwater, *Appl. Phys. Lett.*, submitted.
60. M. M. May, H. J. Lewerenz, F. Dimroth, D. Lackner, and T. Hannappel, submitted.
61. L. L. Kazmerski, *J. Electron Spectros. Relat. Phenomena*, **150**, 105–135 (2006).
62. S. Trasatti, *Pure Appl. Chem.*, **58**, 955–966 (1986).
63. S. Baranovski and O. Rubel, Ch. 2 in " *Charge Transport in Disordered Solids with Applications in Electronics*", John Wiley & Sons, Ltd, Chichester, UK, (2006).
64. H. J. Lewerenz and T. Bitzer, *J. Electrochem. Soc.*, **139**, L21 (1992)
65. H. J. Lewerenz, T. Bitzer, M. Gruyters, and K. Jacobi, *J. Electrochem. Soc.*, **140**, L44 (1993).
66. H. J. Lewerenz, M. Aggour, C. Murrell, M. Kanis, H. Jungblut, J. Jakubowicz, P. A. Cox, S. A. Campbell, P. Hoffmann, and D. Schmeisser, *J. Electrochem. Soc.*, **150**, E185 (2003).
67. A. J. Bard and M. S. Wrighton, *J. Electrochem. Soc.*, **124**, 1706 (1977).